Maximizing DC-to-Load Efficiency for Inductive Power Transfer

Manuel Pinuela, *Student Member, IEEE*, David C. Yates, *Member, IEEE*, Stepan Lucyszyn, *Senior Member, IEEE*, and Paul D. Mitcheson, *Senior Member, IEEE*

***Abstract*—Inductive power transfer (IPT) systems for transmitting tens to hundreds of watts have been reported for almost a decade. Most of the work has concentrated on the optimization of the link efficiency and has not taken into account the efficiency of the driver. Class-E amplifiers have been identified as ideal drivers for IPT applications, but their power handling capability at tens of megahertz has been a crucial limiting factor, since the load and inductor characteristics are set by the requirements of the resonant inductive system. The frequency limitation of the driver restricts the unloaded *Q*-factor of the coils and thus the link efficiency. With a suitable driver, copper coil unloaded *Q* factors of over 1000 can be achieved in the low megahertz region, enabling a cost-effective high *Q* coil assembly. The system presented in this paper alleviates the use of heavy and expensive field-shaping techniques by presenting an efficient IPT system capable of transmitting energy with a dc-to-load efficiency above 77% at 6 MHz across a distance of 30 cm. To the authors knowledge, this is the highest dc-to-load efficiency achieved for an IPT system without introducing restrictive coupling factor enhancement techniques.**

***Index Terms*—Class-E, inductive coupling, inductive power transfer (IPT), semiresonant, wireless power transfer (WPT).**

I. Introduction

INDUCTIVE power transfer (IPT) without a magnetic core was first proposed by Nikola Tesla to supply wireless mains power over long distances around 100 years ago [1]. Since then, low-power, closely coupled wireless charging methods have been used to power medical implants [2], while the wireless powering of portable devices through charging mats is now available via commercial products [3]. Nonetheless, there has been a resurgence in research interest in wireless power transfer (WPT) for medium range (i.e. tens of centimeter) applications, such as electric vehicle charging through resonant inductive coupling [4]–[7]. A basic IPT systems architecture consists of several modules, as illustrated in Fig. 1. The architecture includes dc power supply units (PSUs), coil driver (i.e. clock generator and power amplifier (PA) having an impedance matching network), transmitting (TX) coil with separation distance *D* from a receiving (RX) coil (measured from the center to center of the coils), an optional rectifier/regulator, and a load. To fully characterize the complete system, the end-to-end efficiency η_{ee} of all the building blocks, from the ac source to the load, can be considered as follows, where the efficiency terms are shown in Fig. 1

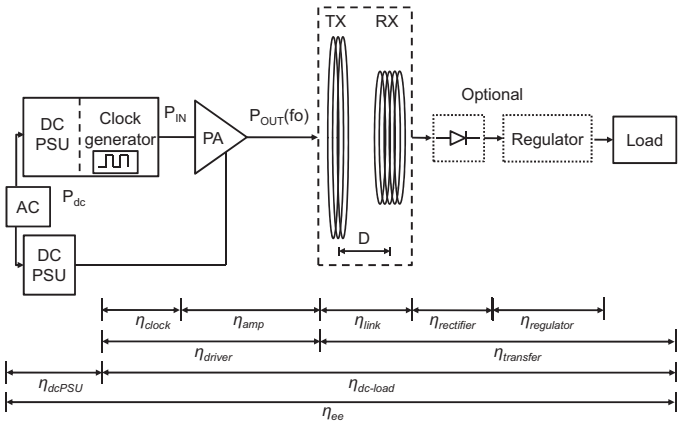

Fig. 1. IPT systems architecture.

$$\eta_{ee} = \eta_{\text{dc-PSU}}\eta_{\text{dc-load}} \tag{1}$$

$$\text{where } \eta_{\text{dc-load}} = \eta_{\text{driver}}\eta_{\text{transfer}} \tag{2}$$

$$\text{and } \eta_{\text{driver}} = \eta_{\text{clock}}\eta_{\text{amp}} \tag{3}$$

where $\eta_{\text{dc-PSU}}$ is the combined efficiency of the dc power supplies, $\eta_{\text{dc-load}}$ is the dc-to-load efficiency, η_{driver} is the efficiency of the driver, η_{link} is the link efficiency, η_{transfer} is the transfer efficiency, η_{clock} is the efficiency of the driver clock, η_{amp} is the efficiency of the PA, $\eta_{\text{rectifier}}$ is the rectifier efficiency, and $\eta_{\text{regulator}}$ is the efficiency of the regulator. This paper focuses on optimizing $\eta_{\text{dc-load}}$ for an IPT system without a rectifier or regulator, i.e., maximizing

$$\eta_{\text{dc-load}} = \frac{P_{\text{load}}}{P_{\text{dc}}} \tag{4}$$

where P_{dc} is the total dc input power to the system (i.e., into the clock and PA) and P_{load} is the real power dissipated in the load.

For many industrial and commercial applications, IPT systems must be capable of achieving a high η_{ee}, while transferring hundreds of watts at submeter distances; otherwise, they will not be adopted. Several approaches for achieving good link efficiencies have been developed by several research groups. The first is to work at relatively low frequencies (tens of kilohertz),

Manuscript received July 6, 2012; accepted August 13, 2012. Date of current version November 22, 2012. This work was supported in part by the European Community's Seventh Framework Program under Grant 223975 and by Project MOBESENS. Recommended for publication by Associate Editor U. K. Madawala.

The authors are with the Department of Electrical and Electronic Engineering, Imperial College London, London, SW7 2AZ, U.K. (e-mail: m.pinuela09@imperial.ac.uk; david.yates@imperial.ac.uk; s.lucyszyn@imperial.ac.uk; paul.mitcheson@imperial.ac.uk).

Color versions of one or more of the figures in this paper are available online at http://ieeexplore.ieee.org.

Digital Object Identifier 10.1109/TPEL.2012.2215887

0885-8993/$31.00 © 2012 IEEE

TABLE 1
IPT SYSTEMS COMPARISON

D [cm]	fo [kHz]	Driver Technology	Coil Technology	Magnetic Material	P_{load} [W]	$\eta_{transfer}$ [%]	$\eta_{dc\text{-}load}$ [%]	η_{ee} [%]	Ref.
0	134	Class-E	Litz wire	No	295	-	-	75.7	[12]
0	240	Class-E	Litz wire	No	3.7	71	-	66	[13]
10	20	H-bridge	Litz wire	Yes	2,000	85	-	-	[6]
10	-	-	-	Yes	3,300	-	-	90	[14]
15	6,700	HF transceiver	Loop + pancake coil	No	-	93	-	-	[15]
15	-	H-bridge	Litz wire	Yes	2,000	95	-	-	[16]
18	145	-	Litz wire	Yes	300-3,000	-	-	90	[17]–[19]
20	4,000	Class-E	Copper wire coil	No	2	-	50	-	[20]
20	20	H-bridge	Power lines	Yes	60,000	80	-	-	[21]
20	20	H-bridge	Power rail	Yes	27,000	-	-	74	[22]
30	3,700	HF transceiver	Surface spiral	No	220	95	-	-	[10]
30	**6,000**	**Class-E**	**Copper pipe coils**	**No**	**95**	-	**77**	**-**	**[our work]**
18-30, 40*	20	H-bridge	-	Yes	3,000	-	-	> 85	[23], [24]
70	7,650	Signal generator	Loop + pancake coil	No	30	75	-	-	[25]
50	13,560	Class-E	Loop + rectangle coil	No	70	85	70**	-	[11]
50	27,000	HF transceiver	Loop + spiral coil	No	40	47	-	-	[8]
100	508.5	Class-D	Litz wire	No	5-35	76	-	-	[26]
200	9,900	Colpitts oscillator	Litz wire	No	60	50	-	15	[9]

*Maximum power transfer distance stated in the cited website [24].
**Calculated based on estimated value of η_{driver} [11].

where efficient driver circuits can be easily realized and by increasing the coupling factor *k* of the system, using field-shaping techniques, for example, by employing metamaterials [8] and ferrite cores [6]. In [6], 2 kW of power was transferred at a distance of 10 cm using Litz wire coils at 20 kHz. The operating frequency was defined by the power handling capabilities of the coil driver, limiting the maximum coil unloaded *Q*-factor to 290. Field-shaping techniques normally occupy useful volume, require heavy materials, employ expensive fabrication techniques, and need a precise coil alignment. These solutions make the field-shaping approach unsuitable for many applications, where the size, weight, and cost of the system are limiting factors.

The second approach relies on transferring energy at the optimum frequency for maximum power transfer given a particular coil size, where the unloaded *Q* is maximized and compensates for the low coupling factor. In the past, this approach was not considered efficient, since low driver efficiency (due to semiconductor losses) dramatically reduced the end-to-end efficiency of the IPT system. An example of this was described by Kurs *et al.* [9], where the use of a 9.9-MHz Colpitts oscillator driver achieved an end-to-end efficiency of only 15%, when the transfer efficiency was 50%. Other attempts at this approach have been successful, with the use of commercially off-the-shelf (COTS) equipment to drive and impedance match the TX coils at frequencies above 3 MHz and with $\eta_{\text{transfer}} = 95\%$, while also reducing the coil losses by using a surface spiral [10].

It is of the utmost importance that consistent, well-defined figures of merit, such as $\eta_{\text{dc-load}}$ and η_{ee}, are used to evaluate IPT systems to allow a straightforward comparison of the different emerging technologies in this field. From the IPT systems architecture in Fig. 1, the transfer efficiency just describes part of the system's efficiency and does not take into account the driver.

Table I shows comparisons of the state of the art in IPT systems. In Table I, η_{transfer}, $\eta_{\text{dc-load}}$, and η_{ee} have been separated out, where possible, to highlight that dc-to-load efficiency can be substantially lower than the transfer efficiency. It is interesting to note that the highest η_{ee} has been demonstrated by all the commercial IPT systems currently available on the market. High efficiencies of $\eta_{ee} = 90\%$ have been achieved at distances of less than 30 cm but with relatively heavy systems (30–40 kg) that use field-shaping ferromagnetic materials. In contrast, a system with frequency tracking and no ferromagnetic materials was used in [11], where an estimated $\eta_{\text{dc-load}} = 70\%$ was calculated. Here, no clear description of the driver's efficiency is given, as it is based on a COTS 50-Ω system with added TX and RX loops. Emphasis was again given to the control of the link and transfer efficiency, rather than the dc-to-load efficiency. Other interesting attempts to increase the end-to-end efficiency have been presented in [12] and [13], where $\eta_{ee} > 60\%$ have been achieved at close proximity.

The challenge then is to realize a high frequency, cost effective, and efficient solution for mid-range IPT in the absence of field-shaping techniques, allowing a light-weight system to be achieved. A system with a TX–RX coil size difference represents a more realistic system, where the receiver size is usually constrained by its application. This system must be able to achieve high efficiency for lower coupling factors, due to the smaller RX coil size. Furthermore, this system must be able to achieve high efficiencies even under situations where perfect alignment is not always achievable (e.g., electric vehicle or wireless sensor charging).

This paper provides an overview of IPT theory, outlining systems architecture, and key component selection that define the system's end-to-end and dc-to-load efficiencies. Cost-efficient coil design, simulations, and measurements to achieve dc-to-load efficiencies above 70% for submeter distances will be

reported. An extensive framework for driver modeling, component selection, and layout considerations to achieve a low-loss, high-frequency dc-RF conversion, capable of delivering more than 100 W at a distance of 30 cm, will be demonstrated. Finally, a full system characterization under different misalignment scenarios is discussed.

II. IPT Theory

With the typical IPT systems architecture, shown in Fig. 1, the driver provides high frequency power to the TX coil, having an unloaded quality factor $Q_{\rm TX}$, which couples as defined by the coupling factor (or coefficient) *k* to the RX coil, having an unloaded quality factor $Q_{\rm RX}$. It is well known that by using receiver (or secondary) resonance and optimizing the load impedance, the link efficiency can be maximized to give

$$\eta_{\rm link} = \frac{k^2 Q_{\rm TX} Q_{\rm RX}}{(1+\sqrt{1+k^2 Q_{\rm TX} Q_{\rm RX}})^2}. \tag{5}$$

As can be seen from (5), the key to achieving high efficiency is to maximize $k^2 Q_{\rm TX} Q_{\rm RX}$. The coil *Q*-factor can be maximized by choosing the correct operating frequency [27]. Analysis on the interactions of these key variables, using both closed-form mathematical expressions and more detailed numerical modeling in MATLAB, has yielded the following underlying principles for optimization [28]:

1) the loop radii should be maximized, in order to maximize the coupling factor;
2) for a given constraint on loop dimensions, there is an optimal frequency, which is approximately the point at which the radiation resistance begins to be significant compared to the skin-effect resistance;
3) the wire radius and the number of coil turns should be as large as possible (bearing in mind that the coils should remain electrically small, to limit the electric field and hence radiation);
4) in the case where the loops are not of equal size, the maximum operating frequency will be mainly determined by the larger of the two coils, also this dictates the lowest self-resonance frequency.

As presented in [12], four different configurations have been widely used for IPT systems. A series resonance can only be used if the parasitic shunt capacitance of the inductor is assumed to be negligible. In contrast, this assumption is not needed for the parallel case, since the parallel resonator capacitor can absorb the parasitic capacitance of the coil. Furthermore, the coupled RX coil is always assumed to be operating at resonance; this way, the equivalent optimal load on the transmitter, reflected from the receiver, will only be resistive, affecting only the damping of the transmitter tank [2].

III. Coil System Design and Characterization

To increase the efficiency of an IPT system, capable of transmitting tens to hundreds of watts at a distance of 30 cm, with perfectly aligned coils, simulations as described in [28] and measurements as described in [29] were undertaken for the TX and RX coils. With this technique, the *Q*-factor was measured through transmission coefficient measurements using two loosely inductive coupled coils as probes. For electromagnetic design reasons, the distance *D* from the center to center of the coils is used. However, it is important to note that the minimum distance between coils is $(D-7)$ cm throughout this work. As mentioned previously, a different sized TX and RX coil was used in the setup; this was thought to be more realistic for most scenarios. The coils were fabricated with copper piping having a 1-cm diameter and 1-mm wall thickness.

After characterizing the coils, the highest Q for both TX and RX coils is found close to 6 MHz, where skin depth is only 27 μm. The maximum unloaded Q value for the five-turn, 20-cm diameter RX coil was $Q_{\rm RX}=1100$ and $Q_{\rm TX}=1270$ for the three-turn, 30 cm TX coil; these matched simulation results when using the following standard expression for the unloaded *Q*-factor of a coil:

$$Q = \frac{\omega_d L}{R_{\rm rad}(\omega_d) + R_{\rm Skin}(\omega_d)} \tag{6}$$

where

$$R_{\rm rad}(\omega_d) = N^2 \eta_o \left(\frac{\pi}{6}\right) (\beta_o(\omega_d) r)^4 \tag{7}$$

$$R_{\rm Skin}(\omega_d) \approx \frac{Nr}{2a}\sqrt{\frac{\omega_d \mu_o}{2\sigma_o}} \tag{8}$$

where ω_d is the driven angular frequency of operation, *L* is the self-inductance of the coil, $R_{\rm rad}(\omega_d)$ is the radiation resistance [30], N is the number of turns of the coil, η_o is the impedance of free space, *r* is the radius of the coil, $\beta_o(\omega_d)=2\pi/\lambda_d$, λ_d is the free space wavelength at the driving clock frequency, *a* is the radius of the copper pipe, σ_o is the low frequency conductivity of copper, and μ_o is the permeability of free space. $R_{\rm Skin}(\omega_d)$ is an approximation of the skin-effect resistance but was calculated in simulations using Butterworth's numerical model [31], which also takes into account proximity effects.

A reconfigurable text fixture was fabricated to hold the coils and allow for reproducible and easily adjustable operating scenarios, as will be described in Section V. Perspex was used for both the stands and the coil spacers, to avoid the generation of eddy currents that could result in measurement errors. The coil spacers helped to maintain a fixed distance of 2 cm between windings, measured from the centers of the pipe, to reduce the proximity effect between turns. The test fixture allows the variation of *D*, transverse offset, and angular misalignment between both coils.

Coupling factor measurements were undertaken to characterize the coil coupling in an array of different scenarios. Measurements were undertaken with different separation distances or against transverse coil offsets *h*, as illustrated in Fig. 2; or transmitter or receiver coil angular misalignment, $\theta_{\rm TX}$ or $\theta_{\rm RX}$, respectively, as illustrated in Fig. 3. For experiments involving transverse offset or angular misalignment, the center-to-center distance was fixed at $D=30$ cm, (the minimum distance between coils is 23 cm). Data from these measurements were also used to predict the operating characteristics, as well as the expected efficiency of the IPT system. The *k* measurements and

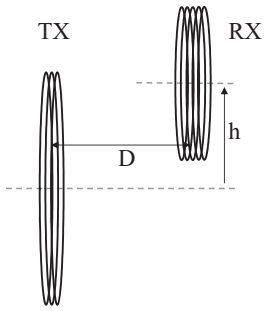

Fig. 2. Experimental setup for distance and transverse offset measurements.

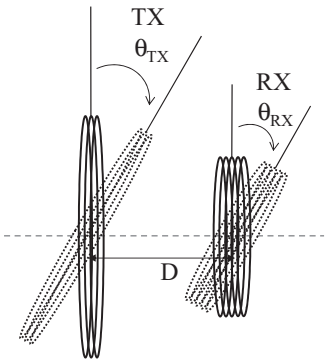

Fig. 3. Experimental setup for angular misalignment measurements.

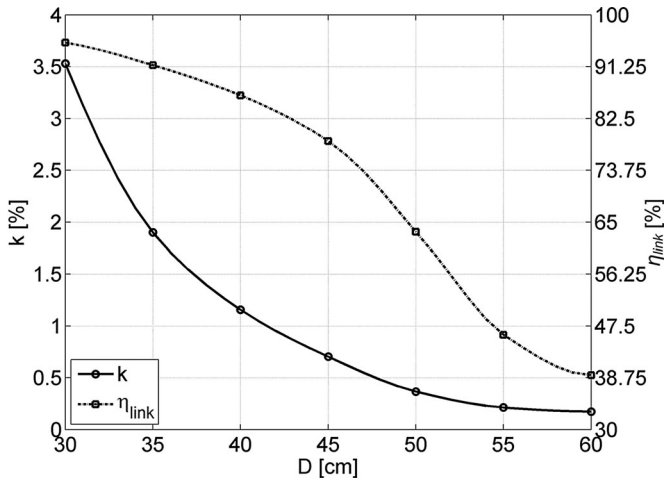

Fig. 4. Measurements of coupling factor against coil separation distance in air, with perfectly aligned coils.

calculations were performed with a well-known voltage transfer technique, as described in detail in [2].

Figs. 4 and 5 show the coupling factor and link efficiency for different distance and transverse offset measurements. Configurations which give rise to the same coupling coefficient are expected to achieve the same efficiency, i.e., perfectly aligned at a separation of $D = 40$ cm should achieve the same efficiency as an offset of $h = 21$ cm at $D = 30$ cm.

Figs. 6 and 7 show k measurement results for TX and RX angular misalignment, respectively. In Fig. 6, while the TX coil angle increases, the distance between both coils reduces enough to compensate for angular misalignment. With the RX

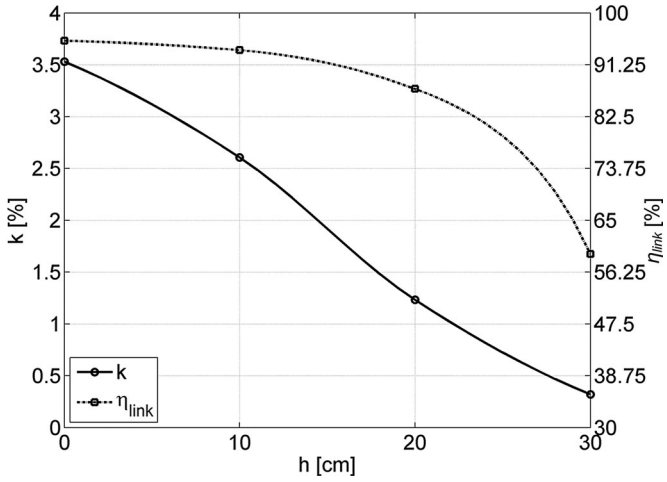

Fig. 5. Measurements of coupling factor against coil transverse offset in air, at a distance of 30 cm.

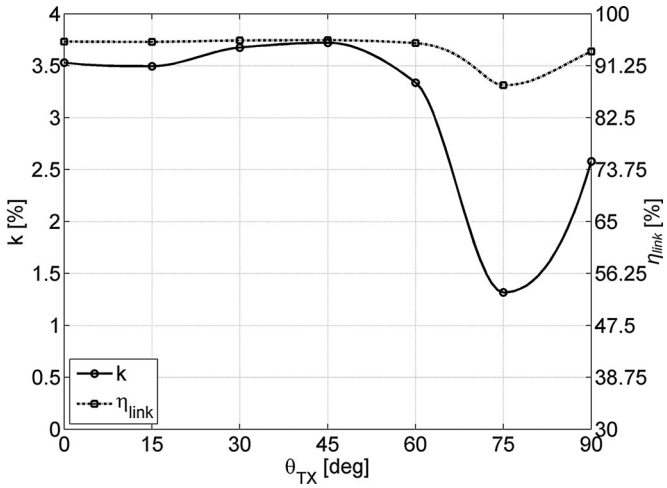

Fig. 6. Measurements of coupling factor against transmitter coil angular misalignment, at a distance of 30 cm.

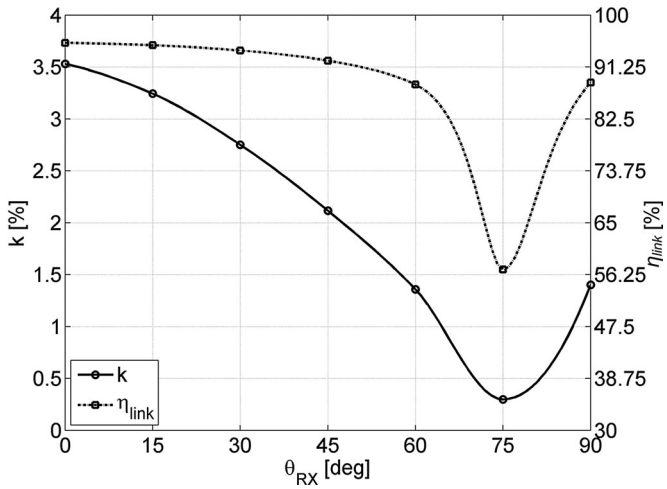

Fig. 7. Measurements of coupling factor against receiver coil angular misalignment, at a distance of 30 cm.

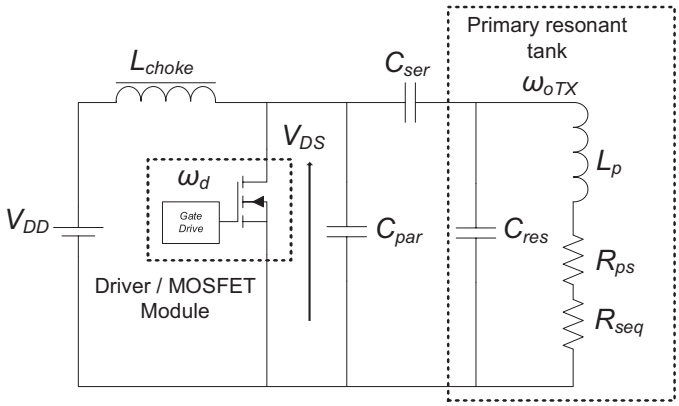

Fig. 8. Semiresonant Class-E topology, with $\omega_d < \omega_{oTX}$.

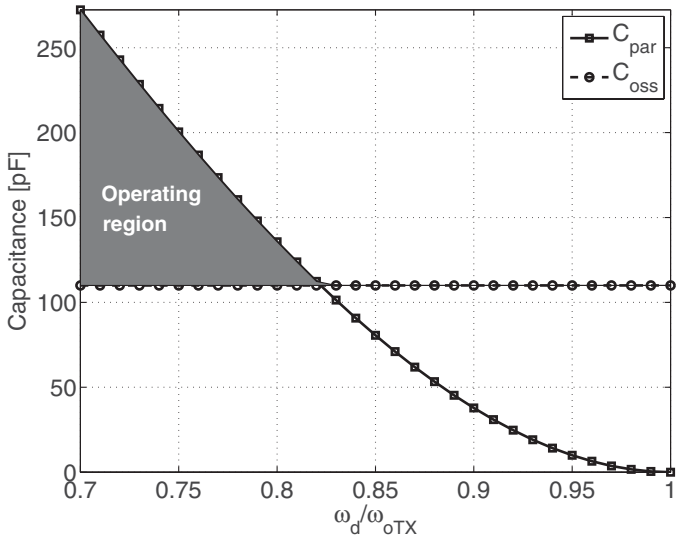

Fig. 9. Simulated $C_{\rm par}$ values against ω_d/ω_{oTX} for Class-E MOSFET selection with a drain–source voltage of 230 V.

coil angle variation, a trough is seen at $\theta_{\rm RX} = 75^\circ$, since this is the point at which the distance between the coils is not enough to compensate for the angular misalignment. These conclusions will be supported in Section V, where a clear correlation between the coupling factor measurements and dc-to-load efficiency will be demonstrated.

IV. Driver Design

Based on the previous coupling factor analysis and measurements of the coils to be used in the later experiments, a high-frequency, high-power driver is required. In a typical IPT system, this is achieved by driving the coils with a 50-Ω loop that is impedance matched to a high-frequency COTS RF transmitter with an output PA. In this typical RF scenario, the maximum power transfer is achieved but not the desired maximum efficiency. The number of stages can be reduced if the 50-Ω impedance is avoided, by integrating the PA and impedance matching circuits into one driver subsystem. This can be achieved by carefully designing a high-efficiency PA capable of high frequency operation. The Class-E amplifier is an ideal solution, since zero-voltage and zero-current switching can be achieved with the appropriate choice of components.

Class-E amplifiers have been designed and used extensively since Sokal and Sokal demonstrated the operational characteristics of their zero-switching PA [32]. It is important to note that even though this PA topology is widely known, designing high PAs capable of working at 100 W and switching at a few megahertz is not a trivial task. This is mainly due to the high power rating and fast switching capabilities that only a suitable power RF MOSFET can achieve, as well as the need to employ high Q capacitors. Furthermore, since an atypical non-50 Ω PA is needed, to avoid additional impedance matching network components and their associated losses, the resonant Class-E topology needs to be modified to suit the coils' characteristics.

To achieve a good efficiency, a semiresonant Class-E topology was selected as a suitable solution [2]. Fig. 8 shows the circuit of a semiresonant Class-E amplifier for the transmitter resonant tank, where the apparent load (represented by the TX coil series resistance R_{ps} and the effective receiver resistance $R_{\rm seq}$) and the apparent inductor (represented by the primary's coil inductance L_p) appear to be larger, thus helping to increase both driver and link efficiencies. This is achieved by tuning the primary resonant tank at a higher resonant frequency ω_{oTX}. This frequency is higher than the receiver's resonant tank driven resonant frequency $\omega_o = \omega_{oRX}$, at which the MOSFET gate driver switches at an operating frequency ω_d, where

$$\omega_{oTX} > \omega_{oRX} \equiv \omega_d. \tag{9}$$

This semiresonant operation also avoids the losses associated with an extra inductor, typically added in series with the TX coil to increase the driver efficiency [12]. Furthermore, as will be demonstrated in the following section, the use of semiresonant operation allows a simple but effective tuning mechanism; by modifying the frequency ratio ω_d/ω_{oTX}, the effective equivalent resistance and inductance of the primary tank can change for different operating scenarios.

Using the results provided in Section III, for an operating scenario with $D = 30$ cm and a perfect coil alignment, PSpice simulations were performed to validate the design equations and design guidelines presented in [2], [33], and [34] but modified to account for semiresonant operation. The IXYSRF IXZ421DF12N100 module, which includes a DE375-102N12A power MOSFET and integrated gate driver, was selected as the best available MOSFET because of its high power handling and nanosecond switching capabilities. This module was also selected due to its relatively low output capacitance $C_{\rm oss}$ at drain–source voltage $V_{\rm DS} = 230$ V, required for 100-W operation. It is important to note that $C_{\rm oss}$ is effectively absorbed by $C_{\rm par}$ and thus is a limiting factor for selecting the maximum ω_d/ω_{oTX} required for high efficiencies. Fig. 9 shows this dependence, where a maximum $\omega_d/\omega_{oTX} = 0.82$, for the set of coils described in the previous section, can be achieved using the selected MOSFET. Working past this threshold would result in a detuned Class-E, incapable of achieving zero voltage, zero current at the time of switching. At this optimal point, for the

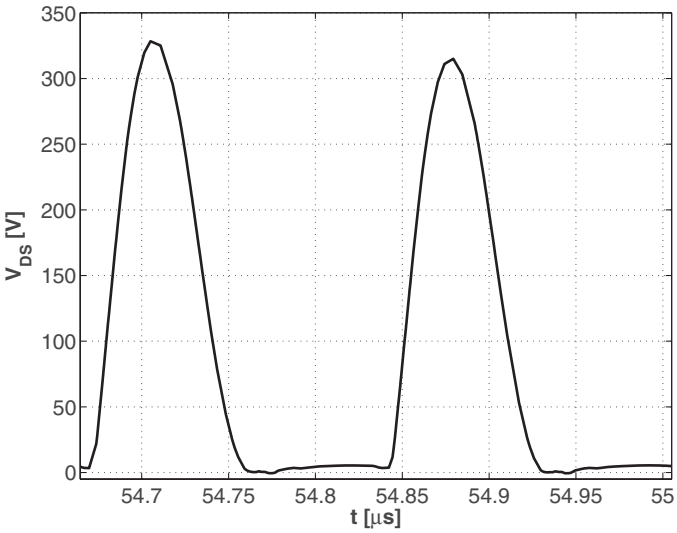

Fig. 10. Simulated drain–source voltage, (PSpice) against time t for the semiresonant Class-E driver.

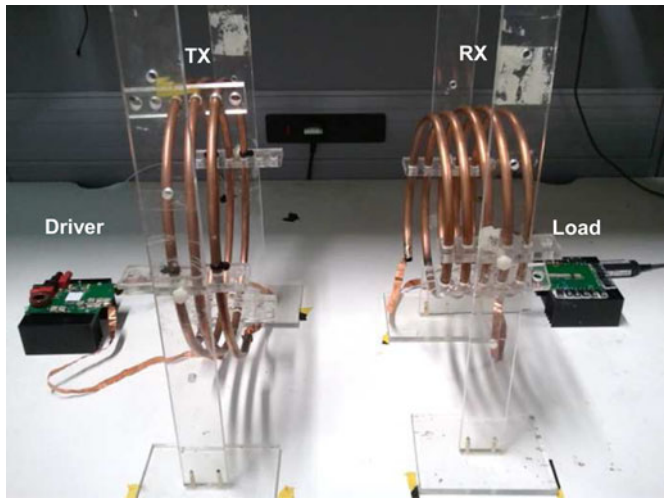

Fig. 11. Perfectly aligned IPT test rig with $D = 30$ cm.

same power, $V_{\rm DS}$ will increase and $I_{\rm DS}$ will decrease, resulting in a greater Class-E efficiency.

During simulations, parasitic inductances and capacitances were added to the model as well as the effective series resistance (ESR) of the capacitors to account, as accurately as possible, for all the losses during operation. Variations of less than 5% in the Class-E capacitor values, compared to those used in the PSpice simulation, were required to achieve a zero-voltage, zero-current crossing and account for the high loaded Q of the resonant circuit due to a low coupling factor. As shown in Fig. 10, a smooth landing of $V_{\rm DS}$ was possible without any negative ringing and an almost ideal Class-E operation was achieved with a simulated dc-to-load efficiency of 80%.

Several key layout considerations had to be taken into account, in order to avoid ground bouncing and ensure good operation. The integrated driver/MOSFET module's input dc bus and gate signal were kept as short as possible; this also applied to ground paths for the module, PSU, and load. To achieve this, ground planes were placed around all components in both layers of the standard low-cost FR-4 substrate, leaving arcing clearances around the tracks and components that were located close to the coil, where voltages as high as 1 kV are present during operation. Similarly, as with the tracks between the driver and MOSFET, all grounding tracks were kept as short as possible to decrease their resistance and inductance, but wide enough to avoid track lifting due to overheating.

In addition to layout considerations, component selection was crucial to enable high frequency operation. A combination of Dielectric Laboratories C40AH capacitor values were employed for $C_{\rm par}$, $C_{\rm ser}$, and both resonator capacitors as they have very high Q and low ESR. Finally, the choke inductor that ensures that only dc current from the PSU flows through the MOSFET was particularly challenging to design, due to the high-current and high-frequency characteristics of the system. A ferrite core was not suitable, due to its poor high-frequency performance. For this reason, an iron powder core was selected, due to its low permeability and stability for high-power applications, as well as high self-resonance frequency.

V. Experimental Results

To fully characterize the practical IPT demonstrator system, shown in Fig. 11, a thorough experimental analysis was performed. The main goal of these experiments was to investigate its behavior in different scenarios, by varying distance, transverse offset, and angular misalignment; this allows a comparison against perfect alignment, to which the system was initially tuned (based on simulations). Furthermore, the results from these experiments were compared against results from frequency tuning the system for each different scenario.

In all experiments, the input voltage $V_{\rm DD}$ was kept constant at 60 V. This allowed sensible values of drain–source voltage to be obtained during operation, to which the output capacitance of the MOSFET is dependant, and helped to avoid replacing $C_{\rm par}$ in each experiment. A constant input dc power for all experiments could not be achieved. This is because, in several scenarios, driver operation was far away from Class-E operation, resulting in high losses during switching that could have degraded or destroyed the MOSFET module.

Due to the fact that the optimal load is very large (e.g. 21 kΩ for the simulated scenario), a noninductive resistor was used. Special considerations where taken to achieve the desired load with a resistive network, because a noninductive resistor capable of handling more than 50 W was not commercially available. Metal film resistors where chosen, given their low inductance behavior at high frequencies and capacity to handle a few watts (enough to withstand up to 100 W, once the load network was made). A major limitation for this type of resistor is that as its resistance and operating frequency increase, the parasitic shunt capacitance also increases and as the resistor temperature increases, its resistance varies. The parasitic capacitance for these resistors was calculated to be 2.8 pF at 6 MHz. This was taken into account when designing the load network and also the selection of the receiver's tuning capacitor. The total capacitance

from the load resistor was absorbed by the calculated tuning capacitance, to ensure receiver resonance, thus avoiding the reflection of capacitive reactance to the transmitter side.

The dc-to-load efficiency of the system was initially measured using Agilent N2783A current probes, but, after several measurements, it was noted that the results were not reflecting the true operation of the circuit. Also, the current probes are not capable of measuring current accurately in the presence of significant electromagnetic noise [35]. The voltage across the load could not be measured with the oscilloscope probe, because the probe's capacitance is 15 pF, enough to detune the receiver coil from resonance. For these reasons, and the fact that the resistor's precise temperature dependence is unknown, an indirect method of measuring the dc-to-load efficiency was implemented. Power was inferred from accurate steady-state heat-sink temperature measurements, since both the driver and the load (including the tuning capacitors) were placed over separated, isolated heat sinks without forced-air cooling. The input dc power was also measured accurately and used together with the RX thermal measurements to calculate the dc-to-load efficiency using the following:

$$\eta_{\text{dc-load}} = \frac{T_{ssRX} - T_{\text{amb}}}{R_{thRX}(T) P_{\text{dc}}} \tag{10}$$

where T_{amb} is the ambient temperature, T_{ssRX} is the heat sink steady-state temperature of the receiving coils, and $R_{thRX}(T)$ is the lumped thermal resistance of the RX load. The temperature measurements were calibrated by applying a known dc power to the RX load until all temperatures reached steady state. Measurements under the same thermal experimental conditions as when the IPT system was tested were performed. Due to the RX load spatial distribution over the heat sink and the fact that the heat sink was positioned with the fins facing downward on the bench, with a 333 K temperature gradient $R_{thRX} = 208$ K/W compared well to the manufacturers 203 K/W. Furthermore, by characterizing the load arrangement, the nonlinear behavior of the heat sink was accounted for, which can be as high as 25%–50% of the dissipated heat, according to [36].

It is important to note that this is a conservative dc-to-load efficiency calculation, since T_{amb} will increase as T_{ssRX} increases, giving a lower $\eta_{\text{dc-load}}$ when compared to the scenario where T_{amb} could be kept constant until the steady state of the system is reached. Even more important is the fact that as the temperature of the resistors increases, the value of the load resistance will start to drift away from its optimal value, drifting away from maximum efficiency.

A. Tuning Procedure

To achieve a semiresonant Class-E operation similar to that observed by simulations, an iterative tuning process had to be performed. This establishes the appropriate values for the driver and the coil capacitors (taking into account their fabrication tolerances) and the coil Q variations (due to metallic objects, such as bench supports, being in close physical proximity to the experiments).

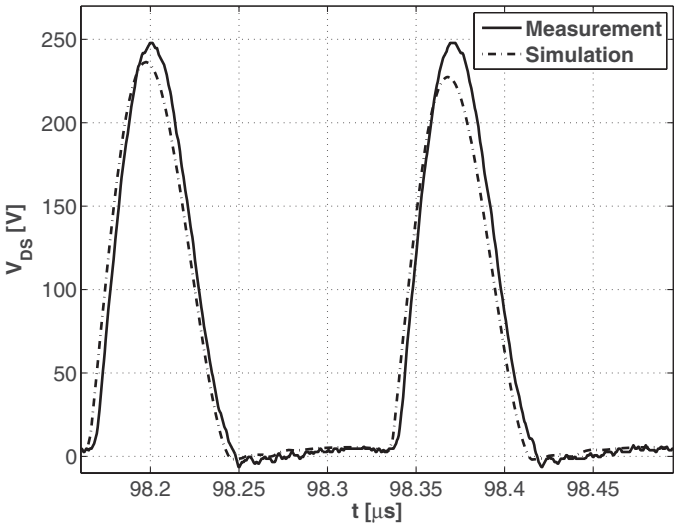

Fig. 12. Drain-to-source voltage against time for the IPT system with a 30-cm separation distance and $P_{\text{dc}} = 90$ W.

First, the receiver resonator's capacitor had to be decreased, to account for the load resistor's equivalent shunt capacitance for correct receiver resonance. With an untuned receiver, the value of the transmitter resonator's capacitor would need to change, to account for the reflected reactance from the receiver onto the transmitter and ensure that semiresonance operation is still present. This changes the ratio of ω_d/ω_{oTX}, which creates the need for retuning C_{par} and C_{ser}. The major limitation of this scenario is that if the ratio ω_d/ω_{oTX} starts to increase, there is a point at which the required C_{par} needed to tune the driver is lower than C_{oss} of the MOSFET, which makes the MOSFET unsuitable for Class-E operation.

Once receiver resonance is obtained, a similar procedure can be followed to achieve zero-switching operation, as described in [33]. Since C_{par} is implemented by an external physical capacitor and C_{oss}, which is dependant on V_{DS}, extra iterations are needed to achieve good operation. As seen from simulations, V_{DS} is a very useful guide to Class-E operation; therefore, tuning the peak-to-peak voltage is as important as achieving zero-voltage, zero-current switching to increase the efficiency [34]. Based on [32], if $V_{\text{DS}} > 3.56\ V_{\text{DD}}$, C_{par} needs to be increased in steps of 5 pF and if $V_{\text{DS}} < 3.56\ V_{\text{DD}}$, it should be decreased by the same amount until the correct V_{DS} is achieved. While doing this, C_{ser} may need a slight adjustment to bring back the driver to zero switching.

Since the load resistance value varies with temperature, several iterations were performed by increasing or decreasing the load resistance by $\pm 5\%$, until a maximum efficiency of 66% was achieved. For each iteration, receiver resonance was achieved and tuning of C_{par} and C_{ser} was performed as previously described. Fig. 12 shows the drain–source voltage (simulated and measured) for the tuned IPT system for an aligned set of coils at a separation distance of 30 cm; the input dc power was 90 W.

While the waveform generated from simulations has a smooth landing, a negative ripple of less than 10 V can be seen when the MOSFET is ON. This negative ripple is generated by a small

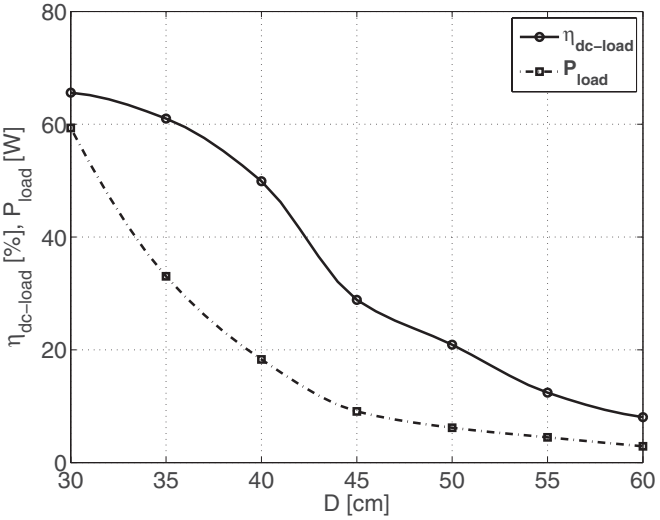

Fig. 13. Measurement of the dc-to-load efficiency against separation distance with fixed clock frequency tuning to aligned 30-cm separation distance scenario.

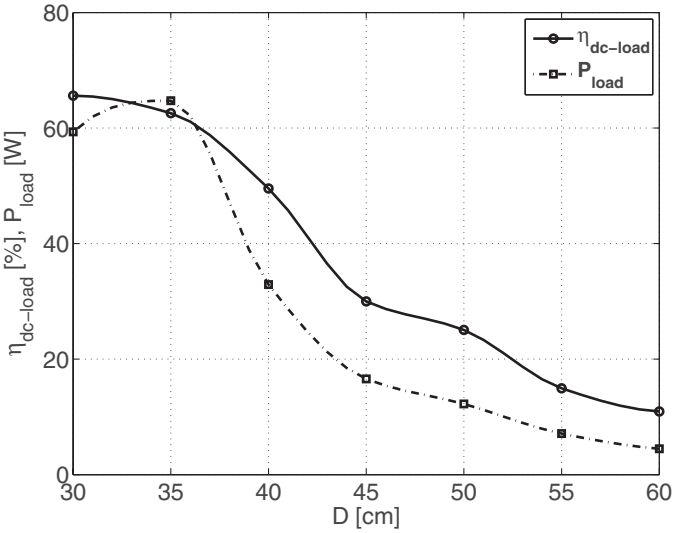

Fig. 14. Measurement of the dc-to-load efficiency against separation distance with clock frequency tuning.

voltage still present at the drain, when the MOSFET is turned ON, due to a higher than expected loaded *Q* for the transmitter resonant circuit. This was the best possible switching achieved with the discrete capacitors available. The higher measured $V_{\rm DS}$ results could be decreased by adding more capacitance to $C_{\rm par}$, but this change was not reflected in a measurable efficiency improvement. Therefore, to decrease the losses in the capacitor (due to ESR), no extra parallel capacitor was added and $V_{\rm DS}$ was left higher than expected in the simulation.

B. System Versatility Analysis

Once the IPT system was optimally tuned to achieve a high efficiency, while being perfectly aligned, measurements with different separation distances were performed to observe the operating capabilities without performing extra tuning. As can be seen in Fig. 13, the distance between the coils was varied between 30 and 60 cm. As *D* increases, the efficiency decreases as the coupling factor decreases, detuning the driver and creating the need for different $C_{\rm par}$ and $C_{\rm ser}$ values to reestablish zero-switching operation.

An easier tuning alternative is to change the operating frequency of the clock, thus relying on the semiresonant operation of the driver. When this was performed, the receiver was no longer in resonance and the transmitter sees a reflected reactance. This extra reactance, in addition to the transmitter's reactance, was enough to improve the tuning of the semiresonant Class-E driver, modifying ω_d/ω_{oTX} and shifting the driver's waveforms closer to zero-switching operation. As seen in Fig. 14, as the clock frequency was altered for each different measurement, the efficiency increased considerably over untuned operation. The dc-to-load efficiency from the clock-frequency tuned version at a 50 cm separation distance was 25%, compared to 20%, as seen in Fig. 13. It is important to note that to achieve this increase in efficiency, a clock frequency change of less than 1% was required.

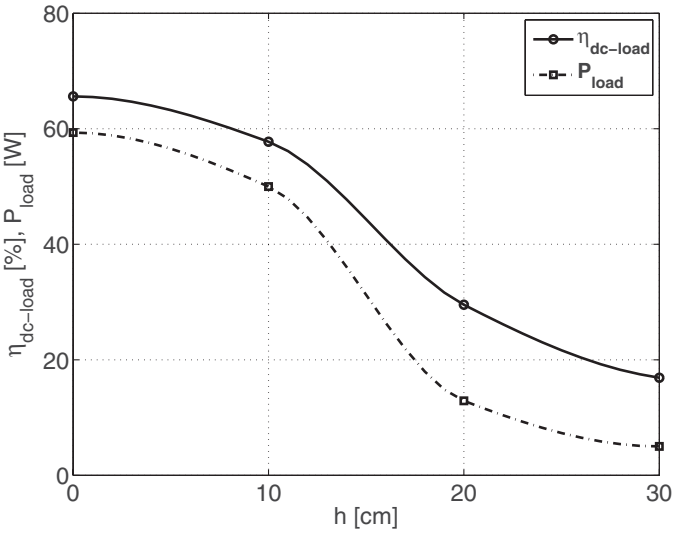

Fig. 15. Measurement of the dc-to-load efficiency against coil transverse offset with fixed clock frequency tuning to aligned 30-cm separation distance scenario.

To analyze the efficiency of the IPT system, for a set of scenarios with different offsets, as shown in Fig. 2, measurements for both the perfectly aligned 30 cm impedance tuning with fixed clock frequency case and with clock frequency tuning were performed. Fig. 15 shows the results for IPT with different coil offsets. In this case, dc-to-load efficiency decreases, following a similar trend as the corresponding *k* measurements from Section III. It can be seen that even with an offset of 10 cm, and no additional tuning, the IPT system performed with a dc-to-load efficiency above 58%.

With clock frequency tuning, as shown in Fig. 16, the dc-to-load efficiency was above 50%, with $h < 14$ cm, and an efficiency increase of 5% was achieved with an offset of 20 cm. Although higher dc-to-load efficiencies could be achieved with tuning the optimal load for each offset, the results presented in this figure demonstrates that efficiencies above 50% can be

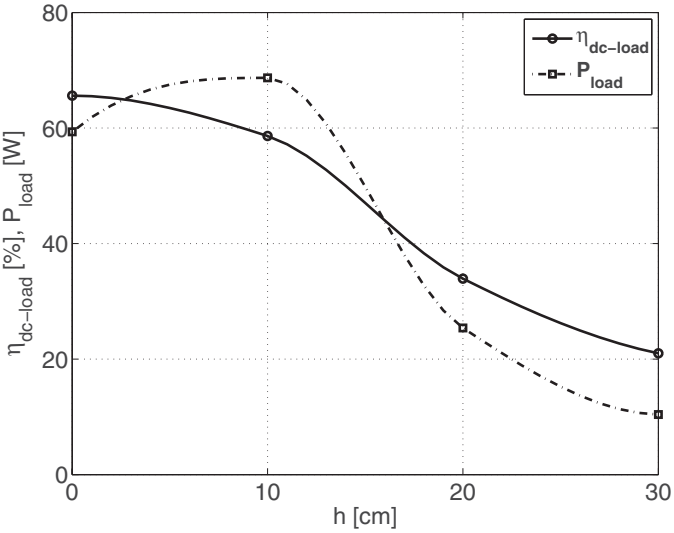

Fig. 16. Measurement of the dc-to-load efficiency against coil transverse offset with only clock frequency tuning.

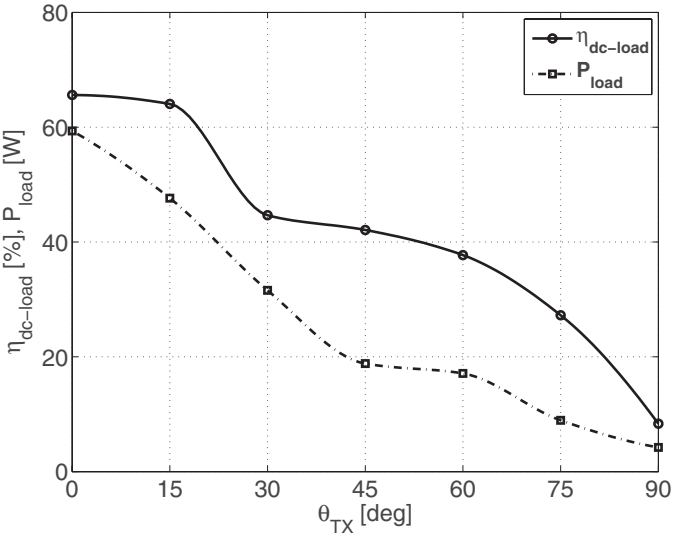

Fig. 17. Measurement of the dc-to-load efficiency against TX coil angle with fixed clock frequency tuning to aligned 30-cm separation distance scenario.

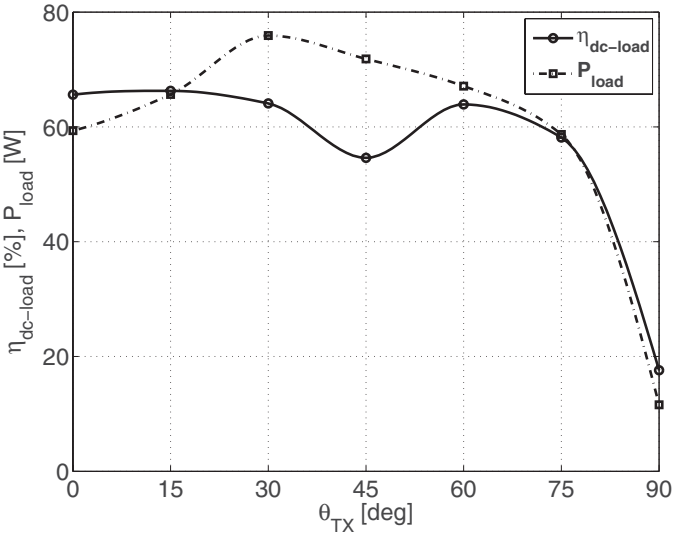

Fig. 18. Measurement of the dc-to-load efficiency against TX coil angular misalignment with clock frequency tuning.

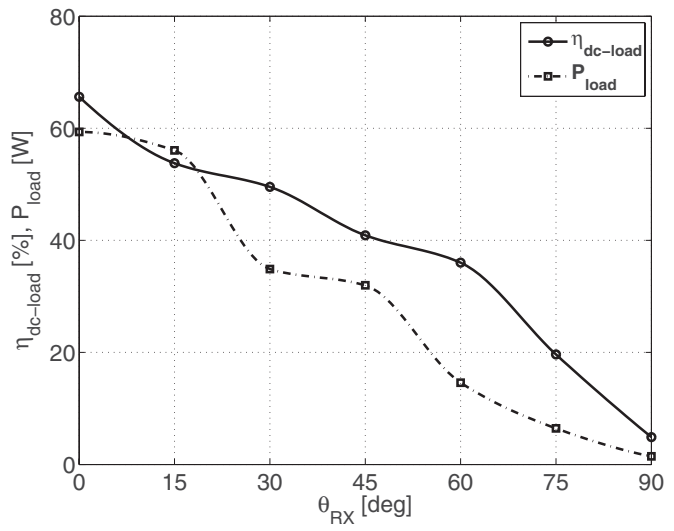

Fig. 19. Measurement of the dc-to-load efficiency against RX coil angular misalignment with fixed clock frequency impedance tuning to aligned 30-cm separation distance scenario.

achieved even at highly misaligned scenarios without the need for load tuning or complex and heavy coupling factor enhancement techniques.

To characterize how the system operates while varying coil misalignment angle θ, in both transmitter and receiver, measurements at a fixed distance of $D = 30$ cm were performed, as shown in Fig. 3. From Figs. 17 and 18, measurements for a varying TX coil angle $\theta_{\rm TX}$ were performed. As predicted, by the coupling factor measurements, a constant high efficiency was achieved for angles below 75° when clock frequency tuning was performed. In contrast, a decrease in efficiency, not clearly linked with *k* was seen with the fixed clock frequency scenario. This is due to the fact that with the fixed clock frequency tuning case, the presence of a larger reflecting load from the receiver influenced efficiency more than with the relatively large and constant coupling factor in the tuning of the IPT system. With the clock frequency tuning scenario, the frequency variation was enough to tune the Class-E and exploit the benefit of almost constant *k*. DC-to-load efficiencies above 60% were achieved for almost all $\theta_{\rm TX} < 72^\circ$ with clock frequency tuning, showing the capabilities of the system to perform in a wide range of transmission angles with a fractional frequency variation of less than 6%.

Finally, measurements with a varying $\theta_{\rm RX}$ were performed, as shown in Fig. 19. The efficiency was almost constant and above 50% up to $\theta_{\rm RX} = 52^\circ$. Above this angle, the efficiency decreased dramatically, as predicted by the coupling factor measurements. A noticeable difference could be appreciated in Fig. 20, with $\theta_{\rm RX} = 45^\circ$, where the dc-to-load efficiency was 56% in the clock frequency tuned case and only 40% in the fixed clock frequency impedance tuned version.

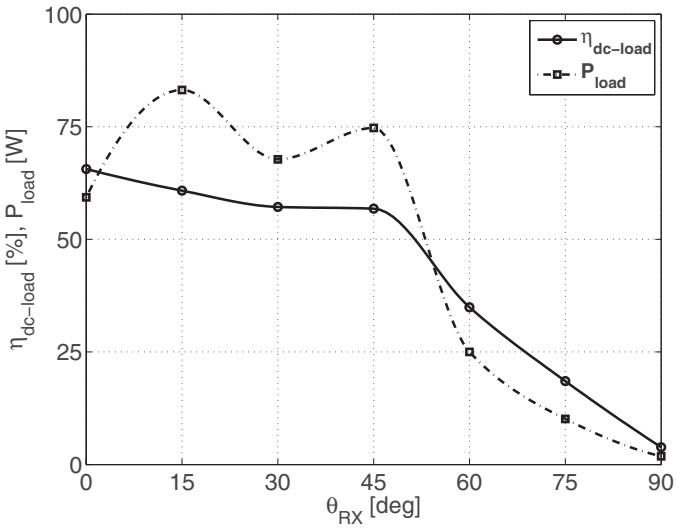

Fig. 20. Measurement of the dc-to-load efficiency against RX coil angular misalignment with clock frequency tuning.

C. Maximum DC-to-Load Efficiency

Finally, the efficiency of the system was increased until the power dissipated by the load resistors caused them to overheat and fail. The highest dc-to-load efficiency achieved with the current prototype design was $\eta_{\text{dc-load}} = 77\%$ for an aligned set of coils at a distance of 30 cm with $P_{\text{load}} = 105$ W. The calculated link efficiency based on the unloaded Q and k measurements was 95%. The dc-to-load efficiency of the system was increased thanks to a higher V_{DD}, which allowed $C_{\text{oss}} = C_{\text{par}}$. This avoided the use of an external capacitor and allowed for a higher ω_d/ω_{oTX}, which increased the apparent driver inductance of the system. To the authors' knowledge, this is the highest dc-to-load efficiency ever presented for an IPT system, without k enhancement techniques.

VI. Conclusion

A comparison of state-of-the-art IPT systems has been given, a clear efficiency analysis is suggested for a meaningful comparison between competing solutions, and key differences between link and dc-to-load efficiencies have been highlighted. An indirect thermal method for measuring P_{load} has been presented for the first time with an IPT system to avoid measurement inaccuracies due to load resistance variations and high external electromagnetic fields in the current measurements. This method was compared against (5) and well-known coupling factor measurements and a clear correlation can be seen, demonstrating the robustness of the efficiency measurement procedure. Low cost, high Q coils, and a complete design and operational analysis of a semiresonant Class-E driver for this IPT system has been described. The driver topology and component selection enabled high-frequency, medium-power, WPT for different transmitter and receiver coil sizes. A detailed transverse offset and angular misalignment characterization demonstrated efficiencies above 50% for transverse offsets up to 14 cm and $\theta_{\text{RX}} = 52^\circ$. Finally, dc-to-load efficiencies of 77% were demonstrated in a perfectly aligned scenario for $D = 30$ cm, having a link efficiency of 95%.

Acknowledgment

The authors would like to thank G. Pappas for his help with experiments, CONACYT (Mexican National Council of Science and Technology), as well as IXYSRF and Dielectric Laboratories for providing useful advice and component samples.

References

[1] N. Tesla, "Apparatus for transmitting electrical energy," U.S. Patent 1 119 732, 1914.
[2] K. V. Schuylenbergh and R. Puers, *Inductive Powering: Basic Theory and Application to Biomedical Systems*. New York: Springer-Verlag, Jul. 2009
[3] S. Y. R. Hui and W. C. Ho, "A new generation of universal contactless battery charging platform for portable consumer electronic equipment," in *Proc. IEEE 35th Annu. Power Electron. Spec. Conf.*, Jun. 2004, vol. 1, pp. 638–644.
[4] D. Schneider, "Wireless power at a distance is still far away [electrons unplugged]," *IEEE Spectrum*, vol. 47, no. 5, pp. 34–39, May 2010.
[5] G. Covic, G. Elliott, O. Stielau, R. Green, and J. Boys, "The design of a contact-less energy transfer system for a people mover system," in *Proc. Int. Conf. Power Syst. Tech.*, 2000, vol. 1, pp. 79–84.
[6] M. Budhia, G. A. Covic, and J. T. Boys, "Design and optimization of circular magnetic structures for lumped inductive power transfer systems," *IEEE Trans. Power Electron.*, vol. 26, no. 11, pp. 3096–3108, Nov. 2011.
[7] A. Karalis, J. D. Joannopoulos, and M. Soljacic, "Efficient wireless non-radiative mid-range energy transfer," *Ann. Phys.*, vol. 323, no. 1, pp. 34–48, 2008.
[8] B. Wang, K. H. Teo, T. Nishino, W. Yerazunis, J. Barnwell, and J. Zhang, "Experiments on wireless power transfer with metamaterials," *Appl. Phys. Lett.*, vol. 98, no. 25, pp. 254101-1–254101-3, Jun. 2011.
[9] A. Kurs, A. Karalis, R. Moffatt, J. D. Joannopoulos, P. Fisher, and M. Soljacic, "Wireless power transfer via strongly coupled magnetic resonances," *Science*, vol. 317, no. 5834, pp. 83–86, Jul. 2007.
[10] S. H. Lee and R. D. Lorenz, "Development and validation of model for 95% efficiency, 220W wireless power transfer over a 30-cm air-gap," *IEEE Trans. Ind. Appl.*, vol. 47, no. 6, pp. 2495–2504, Sep. 2011.
[11] N. Y. Kim and K. Y. Kim, "Automated frequency tracking system for efficient mid-range magnetic resonance wireless power transfer," *Microw. Opt.*, vol. 54, no. 6, pp. 1423–1426, Jun. 2012.
[12] Z. N. Low, R. Chinga, R. Tseng, and J. Lin, "Design and test of a high-power high-efficiency loosely coupled planar wireless power transfer system," *IEEE Trans. Ind. Electron.*, vol. 56, no. 5, pp. 1801–1812, May 2009.
[13] J. J. Casanova, Z. N. Low, and J. Lin, "Design and optimization of a Class-E amplifier for a loosely coupled planar wireless power system," *IEEE Trans. Circuits Syst. II, Exp. Briefs*, vol. 56, no. 11, pp. 830–834, Nov. 2009.
[14] (2012, Feb.). Plugless Power. [Online]. Available: http://www.pluglesspower.com
[15] T. P. Duong and J. W. Lee, "Experimental results of high-efficiency resonant coupling wireless power transfer using a variable coupling method," *IEEE Trans. Microw. Wireless Compon. Lett.*, vol. 21, no. 8, pp. 442–444, Aug. 2011.
[16] J. L. Villa, J. Sallan, J. F. Sanz Osorio, and A. Llombart, "High-misalignment tolerant compensation topology for ICPT systems," *IEEE Trans. Ind. Electron.*, vol. 59, no. 2, pp. 945–951, Feb. 2012.
[17] (2012, Feb.). WiTricity Corporation [Online]. Available: http://www.witricity.com
[18] (2012, May). Delphi wireless charging system [Online]. Available: http://delphi.com/shared/pdf/ppd/pwrelec/wireless-charging-system.pdf
[19] A. Karalis, A. B. Kurs, R. Moffatt, J. D. Joannopoulos, P. Fisher, and M. Soljacic, "Power supply system and method of controlling power supply system," U.S. Patent 20 110 221 278, 2011
[20] L. Chen, S. Liu, Y. Zhou, and T. Cui, "An optimizable circuit structure for high-efficiency wireless power transfer," *IEEE Trans. Ind. Electron.,* vol. 60, no. 1, pp. 339–349, Jan. 2013.
[21] S. Ahn and J. Kim, "Magnetic field design for high efficient and low EMF wireless power transfer in on-line electric vehicle," in *Proc. 5th Eur. Conf. Antenn. Propag.*, Apr. 2011, pp. 3979–3982.

[22] J. J. Huh, S. W. Lee, W. Y. Lee, G. H. Cho, and C. T. Rim, "Narrow-width inductive power transfer system for online electrical vehicles," *IEEE Trans. Power Electron.*, vol. 26, no. 12, pp. 3666–3679, Dec. 2011.
[23] (2012, Feb.). Qualcomm [Online]. Available: http://www.qualcomm.com 2013.
[24] (2012, Feb.). HaloIPT [Online]. Available: http://www.haloipt.com/#n_home-intro
[25] A. P. Sample, D. A. Meyer, and J. R. Smith, "Analysis, experimental results, and range adaptation of magnetically coupled resonators for wireless power transfer," *IEEE Trans. Ind. Electron.*, vol. 58, no. 2, pp. 544–554, Feb. 2011.
[26] J. Garnica, J. Casanova, and J. Lin, "High efficiency midrange wireless power transfer system," in *Proc. IEEE MTT-S Int. Microw. Workshop Series Innovat. Wireless Power Transmiss.: Technol., Syst., Appl.*, May 2011, pp. 73–76.
[27] D. C. Yates, A. S. Holmes, and A. J. Burdett, "Optimal transmission frequency for ultralow-power short-range radio links," *IEEE Trans. Circ. Syst. I, Reg. Papers*, vol. 51, no. 7, pp. 1405–1413, Jul. 2004.
[28] M. Pinuela, D. C. Yates, P. D. Mitcheson, and S. Lucyszyn, "Maximising the link efficiency of resonant inductive coupling for wireless power transfer," presented at the 1st Int. Workshop Wireless Energy Transp. Harvest., Eindhoven, The Netherlands, Jun. 2011
[29] D. Kajfez, S. Chebolu, M. R. Abdul-Gaffoor, and A. A. Kishk, "Uncertainty analysis of the transmission-type measurement of Q-factor," *IEEE Trans. Microw. Theory Tech.*, vol. 47, no. 3, pp. 367–371, Mar. 1999.
[30] C. A. Balanis, *Antenna Theory: Analysis and Design*, 3rd ed. New York: Wiley, 2005.
[31] S. Butterworth, "On the alternating current resistance of solenoidal coils," *Proc. Roy. Soc. London. Series A*, vol. 107, no. 744, pp. 693–715, Apr. 1925.
[32] N. O. Sokal and A. D. Sokal, "Class E-A new class of high-efficiency tuned single-ended switching power amplifiers," *IEEE J. Solid-State Circuits*, vol. 10, no. 3, pp. 168–176, Jun. 1975.
[33] N. O. Sokal, "Class-E RF power amplifiers," *QEX Commun. Quart.*, no. 204, pp. 9–20, Jan. 2001
[34] M. W. Vania, "PRF-1150 1kW 13.56 MHz Class E RF generator evaluation module," Directed Energy, Inc., Tech. Note 9200-0255 Rev. 1, 2002
[35] "Agilent N2780A/B, N2781A/B, N2782A/B, and N2783A/B current probes, user's and service guide," Agilent Technologies Inc., Santa Clara, CA, 2010
[36] S. Rea and S. West, "Thermal radiation from finned heat sinks," *IEEE Trans. Parts, Hybrids, Packag.*, vol. 12, no. 2, pp. 115–117, Jun. 1976.

Manuel Pinuela (S'12) received the B.Sc. degree in electrical and electronic engineering from the National Autonomous University of Mexico (UNAM), Mexico City, Mexico, in 2007, and received the Gabino Barrera Medal, awarded to the highest GPA of his class. He is currently working toward the Ph.D. degree at Imperial College London, U.K.

From 2006 to 2009, he worked in industry, holding electronic design and project engineer roles for companies focused on oil and gas services in both Mexico and the US. His research interests are in wireless power transfer, RF power amplifiers and RF front-end circuits.

David C. Yates (M'03) received the M.Eng. degree in electrical engineering and the Ph.D. degree from Imperial College London, London, U.K., in 2001 and 2007, respectively.

His doctoral research was focused on ultralow-power wireless links. He is currently a Research Associate with the Circuits and Systems Group, Department of Electrical and Electronic Engineering, Imperial College London. His research interests include ultralow power analog and RF circuits for sensor networks, antenna array systems, and wireless power.

Stepan Lucyszyn (M'91–SM'04) received the Ph.D. degree in electronic engineering from King's College London, University of London, London, U.K., and the D.Sc. (higher doctorate) degree from Imperial College London, London, in 1992 and 2010, respectively.

He is currently a Reader (Associate Professor) in millimeter-wave electronics and the Director of the Centre for Terahertz Science and Engineering, Imperial College London. After working in industry as a Satellite Systems Engineer for maritime and military communications, he spent the first 12 years researching microwave and millimeter-wave RF integrated circuits/microwave integrated circuits, followed by RF microelectromechanical system technologies. He has authored or coauthored approximately 135 papers and 11 book chapters in applied physics and electronic engineering, and delivered many invited presentations at international conferences.

Dr. Lucyszyn has served as an Associate Editor for the *IEEE/ASME Journal of Microelectromechanical Systems*. In 2011, he was the Chairman of the 41st European Microwave Conference, held in Manchester, U.K. In 2005, he was elected a Fellow of the Institution of Electrical Engineers, U.K., and a Fellow of the Institute of Physics, U.K. In 2008, he was invited as a Fellow of the Electromagnetics Academy, USA. In 2009, he became an IEEE Distinguished Microwave Lecturer for 2010–2012.

Paul D. Mitcheson (SM'12) received the M.Eng. degree in electrical and electronic engineering and the Ph.D. degree from Imperial College London, U.K., in 2001 and 2005, respectively.

He is currently a Senior Lecturer with the Control and Power Research Group, Electrical and Electronic Engineering Department, Imperial College London. He has research interests in micropower generators and their associated power electronics. He is currently investigating adaptive tuning of energy harvesters using switch-mode electronics and optimised interfaces for piezoelectric harvesters. He has a parallel stream of work in wireless power transfer and RF energy harvesting.